COMPUTER-AIDED CIVIL AND INFRASTRUCTURE ENGINEERING

Computer-Aided Civil and Infrastructure Engineering **00** (2014) 1–20

Identification, Model Updating, and Validation of a Steel Twin Deck Curved Cable-Stayed Footbridge

Oreste S. Bursi*, Anil Kumar & Giuseppe Abbiati

DICAM, Department of Civil, Environmental and Mechanical Engineering, University of Trento, Trento, Italy

&

Rosario Ceravolo

DISEG, Department of Structural, Geotechnical and Building Engineering, Politecnico di Torino, Torino, Italy

Abstract: *To perform a realistic reliability analysis of a complex cable-stayed steel footbridge subject to natural hazard and corrosion, this article addresses a rational process of modeling and simulation based on identification, model updating, and validation. In particular, the object of this study is the Ponte del Mare footbridge located in Pescara, Italy; this bridge was selected as being a complex twin deck curved footbridge because it is prone to corrosion by the aggressive marine environment. With the modeling and simulation objectives in mind, a preliminary finite element (FE) model was realized using the ANSYS software. However, uncertainties in FE modeling and changes during its construction suggested the use of experimental system identification. As a result, the sensor location was supported by a preliminary FE model of the footbridge, although to discriminate close modes of the footbridge and locate identification sensor layouts, Auto Modal Assurance Criterion (AutoMAC) values and stabilization diagram techniques were adopted. Modal characteristics of the footbridge were extracted from signals produced by ambient vibration via the stochastic subspace identification (SSI) algorithm, although similar quantities were identified with free-decay signals produced by impulse excitation using the ERA algorithm. All these procedures were implemented in the Structural Dynamic Identification Toolbox (SDIT) code developed in a MATLAB environment. The discrepancies between analytical and experimental frequencies led to a first update of the FE model based on Powell's dog-leg method that relied on a trust-region approach. As a result, the identified FE model was capable of reproducing the response of the footbridge subject to realistic gravity and wind load conditions. Finally, the FE was further updated in the modal domain, by changing both the stationary aerodynamic coefficients and the flutter derivatives of deck sections to take into account the effects of the curved deck layout.*

*To whom correspondence should be addressed. E-mail: *Oreste.Bursi@ing.unitn.it*.

DOI: 10.1111/mice.12076

1 INTRODUCTION

1.1 Background and motivation

Cable-stayed bridges (CSBs) and footbridges (CSFs) have gained much popularity in the last few decades, because their advantages have become generally known worldwide (Swensson, 2012; Strasky, 2011). These advantages can be summarized as follows: (1) deck bending moments are greatly reduced by load transfer to the stay cables; (2) ease of construction due to the same flow of forces present during free-cantilever construction stages as after completion; (3) inherent stiffness of cable-stayed bridges is greater than that of suspension bridges, because especially for longitudinally eccentric loads, the main cables of a suspension bridge find a new equilibrium configuration without increase of cable stresses, whereas stay cable stresses always increase under new loads; (4) eigenfrequencies of cable-stayed bridges, including the torsion frequency which are important for the aerodynamic safety against flutter, are significantly higher than those of suspension bridges.

Nowadays, the economic main cable-stayed span ranges between 100 m with one tower and 1,100 m with two towers. Some examples include (1) the Lerez Bridge (Troyano et al., 1998) with a single inclined tower; (2) the Safti link bridge (Brownjohn and Xia, 2000) characterized by a curved deck and a single offset pylon; and (3) twin curved deck bridges (Gentile et al., 2004) and twin deck curved footbridges (Ceravolo et al., 2012). Nonetheless, their complex shapes increase difficulties in accurate structural modeling and simulation; in addition, slender footbridges are very sensitive to dynamic phenomena induced by wind and pedestrian loadings, and this characteristic is made even worse by their inherent scarce damping properties (Simiu and Scanlan, 1996; Dallard et al., 2001). Due to these dynamic properties, they are often equipped with damper devices and/or tuned mass dampers that bring the design complexity to an even higher level.

Hence, a valid/reliable finite element (FE) model of a cable-stayed footbridge is typically required to perform sensitivity studies, simulating the actual behavior under extreme winds and/or traffic loading; to carry out checks following high cycle fatigue loads due to traffic; to predict their reliability during their life span, for maintenance and repair planning (Khelifa and Guessasma, 2013).

Along these lines several studies used the ANSYS™ software (ANSYS, 2007) to set up FE models and analyze CSB case studies (Brownjohn and Xia, 2000; Magalhães et al., 2008). This software uses the Ansys Parametric Design Language (APDL) tool that makes it convenient for large structures. Structural System Identification and relevant test design, see Adeli and Jiang (2006) among others, is challenging for complex CSBs. They can show several coupled and close modes that require special methods such as Auto Modal Assurance Criterion (AutoMAC) and stability diagram techniques, to discriminate between modes and to design sensor locations (Allemang, 2002; Carden and Brownjohn, 2008; Hazra et al., 2012). Techniques that help in deriving model properties from vibration data and show changes in structural properties with time, are both the eigenvalue realization algorithm (ERA) and the stochastic subspace identification (SSI) procedures (Juang and Pappa, 1984; Van Overshee and De Moor, 1996), and also more recently adopted time–frequency techniques (Ceravolo, 2009; Ceravolo et al., 2012; Hazra et al., 2012).

Due to limitations of FE modeling applied to complex structures, we know that FE models can be improved using experimental data from the identification process. In this respect, model updating approaches based on sensitivity (Brownjohn and Xia, 2000; Moaveni et al., 2009) and Powell's dog-leg (DL) techniques (Molinari et al., 2009; Savadkoohi et al., 2011) have shown advantages. The updated FE model of CSBs should be validated under typical load conditions. The case of CSBs subjected to wind loads requires special consideration owing to aerodynamic phenomena; therefore, correct modeling of both stationary aerodynamic coefficients and flutter derivatives is needed. Although some authors adopt values relevant to aerodynamic coefficients from bridges with similar deck sections, see for instance He et al. (2007), it is certainly more appropriate to define aerodynamic coefficients directly from wind-tunnel tests (Zasso et al., 2009). The problem of deck curvature should also be considered, but the available literature is limited (Zhu et al., 2002a,b).

1.2 Scope

Though several papers treat special aspects of modeling and simulations of CSBs and CSFs, there are still margins of improvement to some aspects of FE modeling, identification, model updating, and validation of complex curved cable-stayed steel footbridges.

Moreover, for such bridges, reliability analyses based on FE models under severe wind loads and steel corrosion are rare. These effects were the target of the research project HITUBES funded by the European Union (Bursi and Kumar, 2011). In particular, such issues represent basic aspects of footbridge analysis and are the subject that this work explores further, although the relevant reliability analysis will be presented afterward. This article follows the flowchart of Figure 1, which summarizes the conceptual step sequence aimed at obtaining an updated FE model of a cable-stayed bridge/footbridge validated for dynamic simulations; it is organized as follows. First, Section 2 contains a brief description of both the case study and the preliminary FE model, built with the ANSYS software. Second, Section 3 provides information on identification techniques and relevant results. The FE model updating of the footbridge is presented in Section 4 on the basis of modal frequency data. Furthermore, Section 5 describes the implementation of aerodynamic properties on an accurate FE model based on experimental aerodynamic characteristics. Then, the validation of the resulting enhanced FE model is presented in Section 6 through time history analyses accounting for turbulence and skewed wind. Last, conclusions are drawn and summarized.

2 THE CASE STUDY PONTE DEL MARE

2.1 Description of the case study

The Ponte del Mare CSF is located in Pescara at the mouth of the Pescara River close to the sea, in the center of Italy. The bridge has two curved decks sustained by cables connected to a tilted mast. The outer deck is

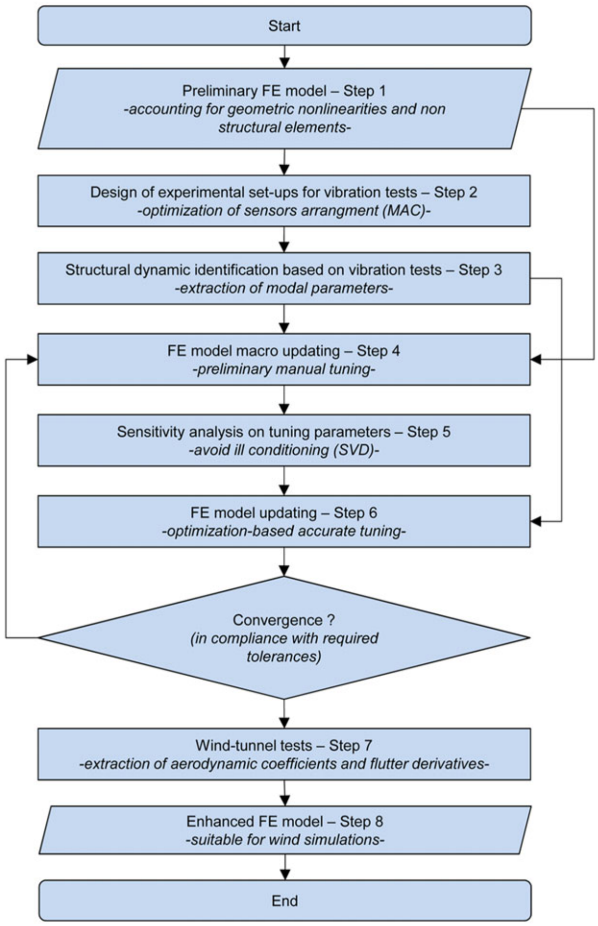

Fig. 1. Conceptual step sequence of FE model updating aimed at producing FE models of cable-stayed bridges and footbridges suitable for dynamic simulations.

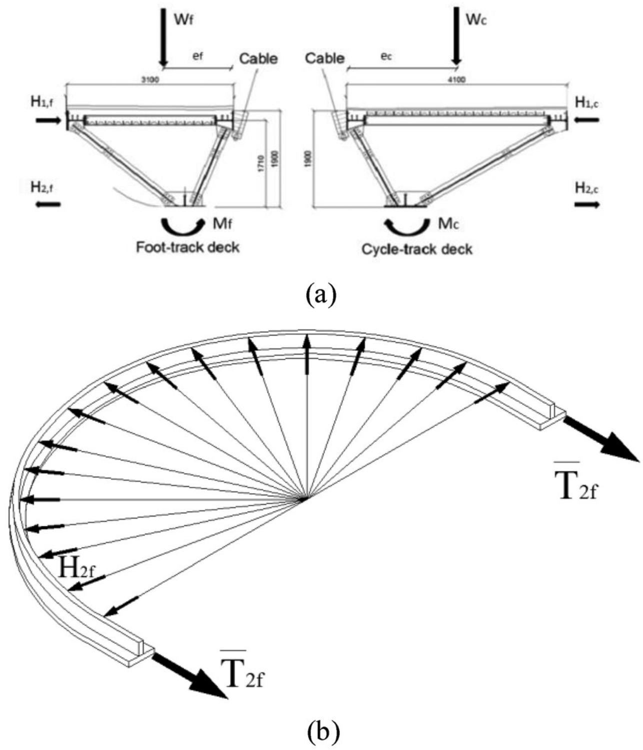

Fig. 2. The Ponte del Mare footbridge: (a) free body diagrams of both foot-track and cycle-track decks; (b) curvature effect on the bottom chord of the foot-track deck.

for pedestrians and the inner is for cyclists; both decks have constant radius, of approximately 80 m and 100 m, and their lengths are 173 m and 148 m, respectively. The two decks are spatial steel-concrete trusses connected to two prestressed concrete access ramps. The two sections of the footbridge are shown in Figure 2a. The mast is of steel filled with concrete and rises between the foot-track and the cycle-track decks, with inclination about 11° with respect to the vertical; two cables anchor the top of the mast to the ground. Due to the mast location within decks, see Figure 3a, and the relevant eccentricities e_f and e_c of typical vertical loads W_f and W_c, see Figure 2a, overturning moments arise on both decks equilibrated by horizontal forces $\mathbf{H}_{2,\mathrm{f}}$ and $\mathbf{H}_{2,\mathrm{c}}$, respectively. According to Figure 2b, the bottom chord of the foot-track deck fixed at both abutments and subject to horizontal forces $\mathbf{H}_{2,\mathrm{f}}$, experiences a tensile force $\bar{\mathbf{T}}_{2,\mathrm{f}}$ owing to curvature effects. As a result, both bottom and top chords of decks are subjected to axial loads of opposite sign. For instance, the bottom chord of the foot-track deck is subject to tensile loading while that of the cycle-track deck is subject to compressive loading. The opposite trend happens for top chords (Ceravolo et al., 2012).

To ensure safety requirements under premature aeroelastic instability owing to wind and to mitigate pedestrian vibration, the bridge was provided with a passive control system. It is based on viscous fluid dampers and aimed at providing positive damping, although limiting changes both in modal frequencies and shapes. The design included eight devices all endowed with viscous fluid damping and some with spring in series; in particular, three damper types, A, B, and C, with differing parameter values as listed in Table 1, were installed at the locations shown in Figure 3a. Dampers of types B and C are illustrated in Figures 3b and c.

The footbridge was monitored for a year and a half from December 2009, with the distributed sensor system defined in Figure 4. The monitoring system consisted of eight accelerometers, four resistance thermometers, and two anemometers.

During one of the more extreme events, on December 25, 2009, accelerations were recorded owing to NS wind excitation from the sea. Accelerations reached 0.4

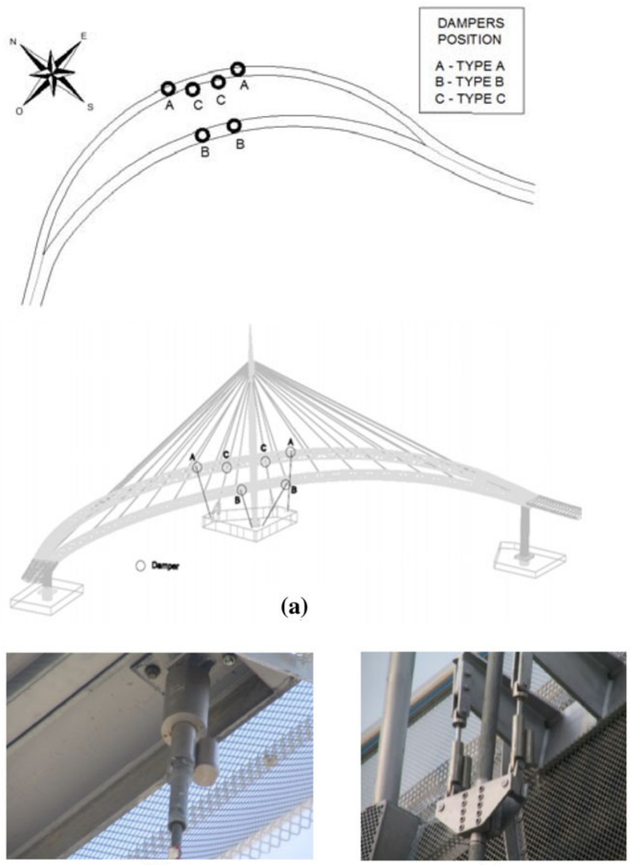

Fig. 3. (a) Passive control system; (b) damper type B; (c) damper type C.

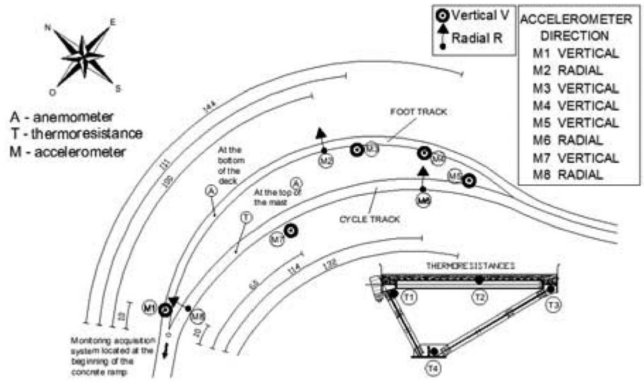

Fig. 4. Structural health monitoring system.

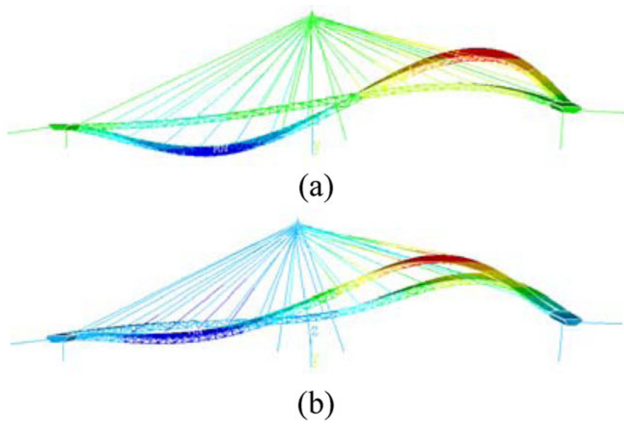

Fig. 5. (a) First mode shape; (b) second mode shape.

Table 1
Damper characteristics

	Damper A	*Damper B*	*Damper C*
Type	Elastic-viscous	Elastic-viscous	Viscous
Units	2	2	2+2
Damping constant	128.0 kNs/m	349.0 kNs/m	794.2 kNs/m
Spring stiffness	127.6 (±5%) kN/m	127.6 (±5%) kN/m	-

m/s^2 at the foot-deck track although at the top of the mast the maximum wind speed recorded was 28.0 m/s.

2.2 The preliminary FE model of the footbridge

The high geometrical complexity of the Ponte del Mare footbridge characterized by 3D bending/torsional coupled modes of decks and cable–deck interaction, prevented the setup of a simplified FE model; as a result an accurate 3D FE model was needed. This refined model also served for the footbridge check under high cyclic fatigue loads caused by pedestrians and wind (Bursi and Kumar 2011). As a result and in agreement with step 1 of Figure 1, a preliminary FE model shown in Figure 5, and composed of 27,093 degrees of freedom (DoFs), was developed in the ANSYS software (2007). Beam, shell, and solid elements were used to model accurately both the main steel-concrete decks and the access ramps taking into account only geometrical nonlinearities. In greater detail, the two decks' trusses and the piers, ramps, mast, and rigid connections were modeled using BEAM44 elements. To avoid free vibration solutions dominated by cable-stayed modes, each cable was reproduced with a single geometrically nonlinear LINK8-3D truss element (Brownjohn and Xia, 2000); Moreover, variations in axial stiffness owing to tensile loading were taken into account by means of Dischinger equivalent elastic moduli (Bruno et al., 2008). The two concrete slabs were modeled by means of SHELL63 elements. Each concrete block at the ends was modeled with SOLID45 elements. The dampers

Table 2
Numerical frequencies predicted by ANSYS preliminary FE model

Mode	*Frequency* f_N *(Hz)*
1	0.681
2	1.003
3	1.087
4	1.144
5	1.369
6	1.518
7	1.546
8	1.666
9	1.702

were modeled with ideal linear viscous COMBIN14 elements. The first nine frequencies provided by modal analysis are shown in Table 2, although for brevity, only two corresponding first- and second-mode shapes can be observed in Figure 5. From Table 2, we see how some frequencies are close; although the mode shapes show that the footbridge exhibits complex behavior owing to coupling between bending and torsion, especially for the second mode.

This preliminary FE model set without dampers was used (1) to design the damper system; (2) to design sensor test setups for identification tests described in Section 3.2.

3 STRUCTURAL SYSTEM IDENTIFICATION

3.1 Design of identification test setups

To ensure a reliable identification of the footbridge dynamic properties, a sensor location design was thought necessary in accordance with step 2 of Figure 1. This design was supported by the preliminary FE ANSYS model of the footbridge without dampers devised in Section 2.2. Due to the complexity of the footbridge to be identified, test setups were designed in view of mode decoupling. To this aim, a number of viable sensor configurations were generated and AutoMAC matrices were produced for the first 10 modes of the FE model and for each setup (Allemang, 2002). In this respect, see Figure 6, setups were then selected on the basis of an AutoMAC-based rule; in detail, for each set-up k a score R_k was defined as the out-of-diagonal average modal assurance criterion (MAC) value of Equation (1) where i and j indicate the eigenmodes of the reference FE model respectively, while n is the number of modes considered for the score calculation:

$$R_k = \frac{\sum_{i}^{n} \sum_{j, j \neq i}^{n} MAC(i, j)}{n \cdot (n-1)} \tag{1}$$

The MAC value adopted in Equation (1) is a coefficient analogous to the correlation coefficient in statistics or coherence in signal processing. It compares ordinates of mode shapes from the FE reference model and experimental data and provides a unit value for perfect correlation and zero for uncorrelated orthogonal modes. It reads

$$MAC(\phi_a, \phi_e) = \frac{(\phi_a^T \phi_e)^2}{(\phi_a^T \phi_a) \cdot (\phi_e^T \phi_e)} \tag{2}$$

where ϕ_a and ϕ_e are analytical and experimental mode shape vectors, respectively. The superscript T denotes the transpose. The score R_k was assumed to be a measure of decoupling. The six lowest R_k setup scores selected for experimental tests are listed in Table 3: (1) String setups, see Figure 6a, were intended to capture out-of-plane transverse and vertical modes; (2) Dec setups, see Figure 6b, captured modes characterized by the greatest decoupling; and (3) Carpet setups were devised to identify single deck torsional modes. In addition, the permanent monitoring setup of Figure 4 described in Section 2.1 was used.

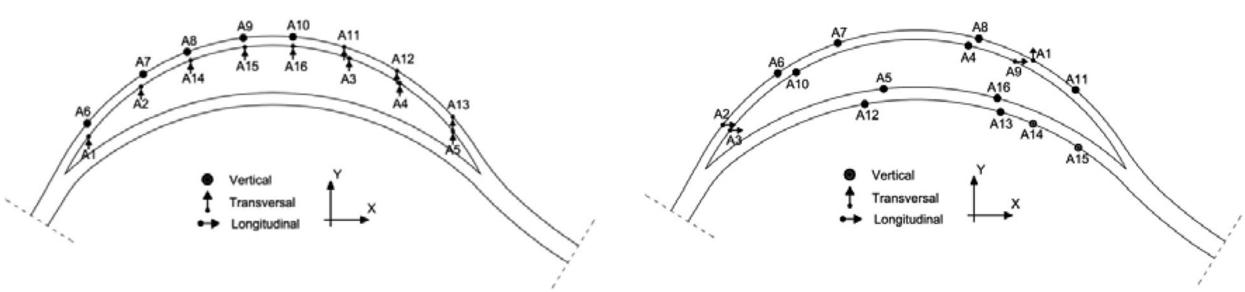

a) Setup String 1 - 16 Channels employed b) Setup Dec 1 - 16 Channels employed

Fig. 6. Experimental setup for system identification tests.

Table 3
R_k scores of the selected six setups

Setup	R_k
String 1 (ST1)	0.1272
String 2 (ST2)	0.2065
Carpet 1 (CP1)	0.1436
Carpet 2 (CP2)	0.2292
Dec 1 (DC1)	0.1250
Dec 2 (DC2)	0.1095

Therefore, it was possible to assemble identified eigenmodes derived from the different setups and acquired at different stages.

The optimal sensor setups were finally validated by a blind test consisting of a fictitious identification procedure based on numerical response signals. This validation procedure was essentially a numerical simulation of the test campaign. Signals were generated by means of the FE ANSYS model of the footbridge and white noise excitation was simultaneously applied to all three directions. A total of 8,000 sample length 16-channel acceleration signals were produced considering only the superposition of the first 10 eigenmodes of the system; the maximum frequency, i.e., 1.984 Hz of the tenth mode, was very small with respect to the sampling frequency $f_s = 64$ Hz. The Newmark method with $\gamma = 1/2$ and $\beta = 1/4$, i.e., the trapezoidal rule (Newmark, 1959), was used to integrate in time the semi-discrete system of equations of motion. The effectiveness of the decoupling achieved by the DC1 setup with respect to the two modes coupled at about 1.50 Hz, see Table 2, can be grasped by means of the Welch transform (Welch, 1967). In detail, Welch Power Spectral Densities (PSDs) of acquisitions generated by means of the FE model relevant to the ST1 setup, see Figure 7a, are compared with the corresponding spectra provided by the setup DC1 shown in Figure 7b.

Peaks in spectral energy distribution, corresponding to the coupled modes at 1.518 and 1.546 Hz, appear more distinct in the case of the DC1 setup.

The identification procedure was carried out adopting the SSI algorithm (Van Overschee and De Moor, 1996). Time history signals provided by the aforementioned trapezoidal rule were downsampled up to 8 and segmented in 10 frames for each one. A subsequent identification session was carried out on each of the 10 frames of about 6,000 samples of length; a system order range between 10 and 20 was considered. For each signal a stabilization diagram was produced using the following stabilization criteria: (1) a variation in natural frequency of less than 2%; (2) a variation in damping less than 1%; (3) a MAC value equal or greater than 0.95. A typical stabilization diagram is shown in Figure 8.

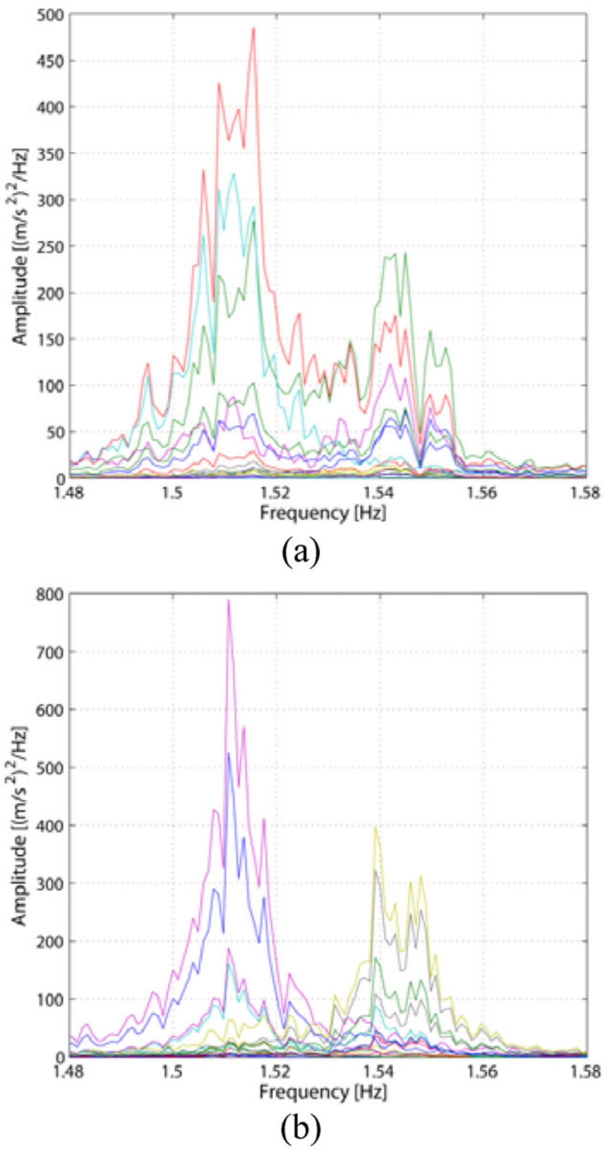

Fig. 7. Welch PSD of the acquisitions generated by means of the FE model relevant to (a) the setup ST1; (b) the setup DC1.

Then, cluster diagrams were defined as depicted in Figure 9 (Carden and Brownjohn, 2008); thus, each of the six set-ups were proven to be effective in terms of decoupling capabilities with respect to the couples of eigenmodes at about 1.50 and 1.70 Hz of Table 2. Along this line, all the first 10 modes of the footbridge FE model were clearly identified; as a result, the proposed setups were employed for the testing campaign described here.

3.2 Identification techniques and results

With regard to identification foreseen in step 3 of Figure 1, the SSI algorithm was used for signals

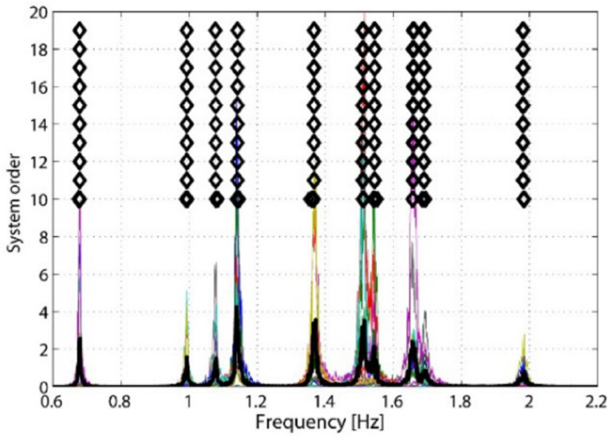

Fig. 8. Stabilization diagram relevant to the acquisition of setup ST1.

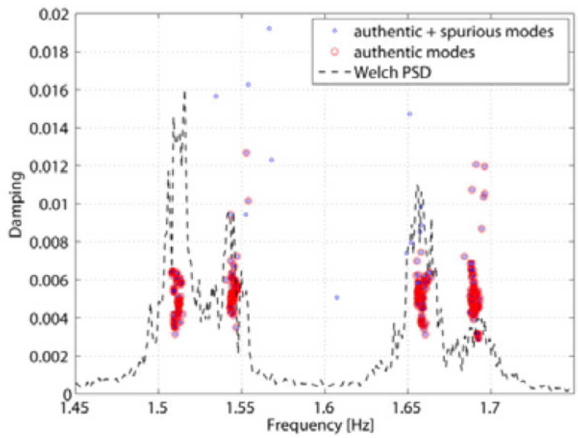

Fig. 9. Cluster diagram of the acquisition relevant to the setup ST1: zoom on the range characterized by the presence of coupled modes.

produced by environmentally induced vibration (Van Overschee and De Moor, 1996), although the ERA was used for free-decay signals generated by impulsive excitation (Juang and Pappa, 1984). Only setups ST1, CP1, and CP2 were exploited with $f_s = 100$ Hz, greater than the sampling frequency assumed for the blind test described in Section 3.1. The first experimental campaign of October 27 and 28, 2009 was conducted for the case without dampers, while the second campaign of October 29 and 30, 2009 faced up the case of dampers. The linear identification was carried out for both cases, without and with dampers. Both the algorithms were coded in the Structural Dynamic Identification Toolbox (SDIT) code (Ceravolo and Abbiati, 2009, 2013), developed in a MATLAB environment (2003). In the case of the Ponte del Mare bridge acquired signals were conditioned by means of antialiasing filters, de-trended and

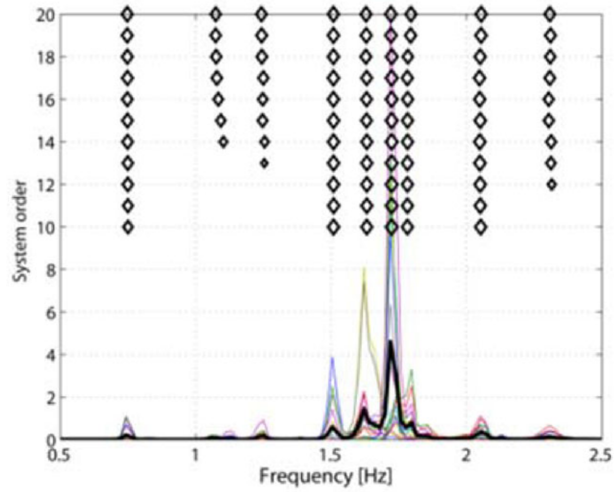

Fig. 10. Stabilization diagrams for the footbridge without dampers relevant to the setup ST1.

subsampled (Ceravolo et al., 2012). After a preanalysis with a Welch power spectral representation, several time–domain identification sessions were carried out. In greater detail, all signals coming from different acquisitions were segmented and a large number of SSI identification evaluations were performed. To eliminate spurious eigenmodes, a cleaning criterion was adopted. The set of mode shapes $\mathbf{V}_i = [\, v_{1,i} \; v_{2,i} \; \ldots \; v_{n,i} \,]$ gathering identification outcomes from each segment ith for different system order values was used to compute the affinity matrix $\mathbf{A}$, defined as

$$\begin{cases} \mathbf{A}_{i,j} = 1, & \text{if} \quad MAC\,(v_i, v_j) \geq 0.95 \\ \mathbf{A}_{i,j} = 0, & \text{if} \quad MAC\,(v_i, v_j) < 0.95 \end{cases} \tag{3}$$

An index of recursion C_i relevant to the mode shape v_i was defined for each row of $\mathbf{A}$, as

$$C_i = \sum_{j=1}^{n} \mathbf{A}_{i,j} \tag{4}$$

Mode shapes characterized by $C_i > 5$ were considered as true; the other ones were discarded as spurious. The threshold value of the index of recursion C_i was proportional to both the segmentation number and to the system order range considered and, in addition, to the quality of acquired signals. According to the blind test based on the same stabilization criteria outlined in Section 3.1, stabilization diagrams were used to classify true eigenmodes up to 2.5 Hz within identification data sets purged from spurious modes. Stabilization diagrams relevant to the first 10 identified modes for the case of the footbridge without dampers are reported in Figure 10; in addition, Figure 11 depicts relevant cluster diagrams for the same identification data set.

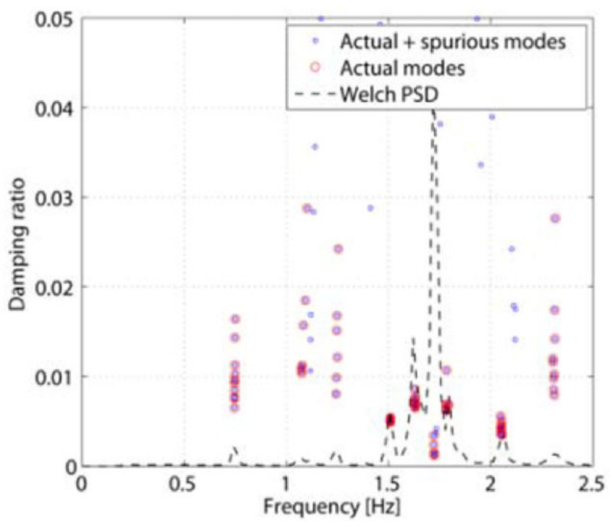

Fig. 11. Cluster diagrams for the footbridge without dampers relevant to setup ST1.

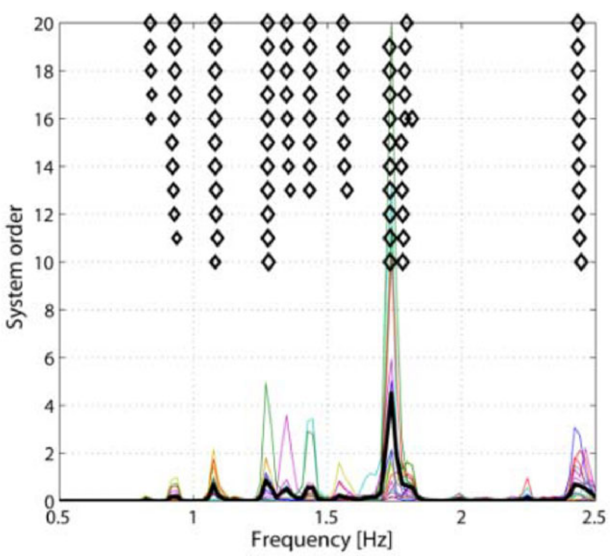

Fig. 12. Stabilization diagrams for the footbridge endowed with dampers relevant to setup ST1.

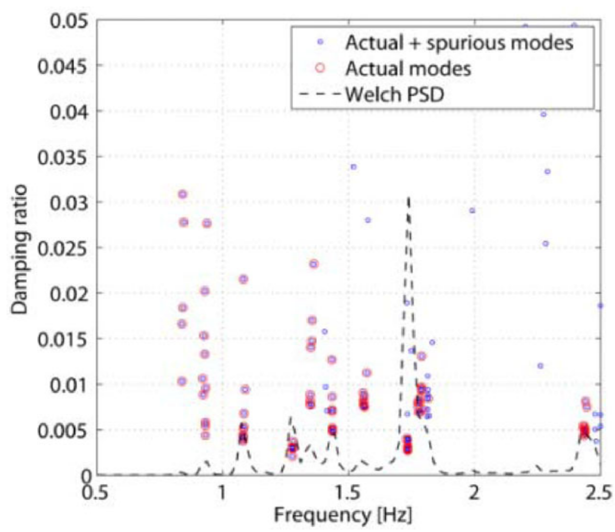

Fig. 13. Cluster diagrams for the footbridge endowed with dampers relevant to setup ST1.

Table 4
Eigenfrequencies f_X and relevant damping ratios in the cases without and with dampers, respectively

	Case w/o dampers		*Case with dampers*	
Mode	*Frequency (Hz)*	*Damping ratio (%)*	*Frequency (Hz)*	*Damping ratio (%)*
1	0.748	1.10	0.92	3.22
2	1.065	1.32	1.08	3.20
3	1.126	1.40	1.34	4.84
4	1.243	1.10	1.27	2.89
5	1.394	1.46	1.44	2.14
6	1.510	1.80	1.55	2.96
7	1.716	1.34	1.73	3.59
8	1.791	1.65	1.80	4.89
9	2.306	1.20	2.43	4.13
10	2.364	0.94	2.53	2.63

Figures 12 and 13 show the stabilization diagrams and the cluster diagrams, respectively, for the footbridge endowed with dampers. Moreover, Table 4 gathers identification results in terms of eigenfrequencies and relevant damping ratios, both for the footbridge without and with dampers.

From Table 4 the reader will note the large frequency discrepancy for the presence of dampers on the first vibration mode.

In particular, we note that a more specific study conducted in the time–frequency domain (Ceravolo, 2009) confirmed on the one hand the results obtained from the SSI algorithm, and on the other, revealed that the footbridge with dampers actually behaves like a threshold system: (1) for low vibration levels, dampers are stationary, so that they act as constraints that stiffen the structure; (2) for high vibration levels, dampers become fully active and, as required at the design stage, do not significantly affect the main design frequency (Ceravolo et al., 2012). Free-decay oscillations induced through a release of masses were considered for the damping identification by means of the ERA (Juang and Pappa, 1984). Subsequent mode shapes relevant to the first identified mode for the footbridge cases without and with dampers are depicted in Figure 14.

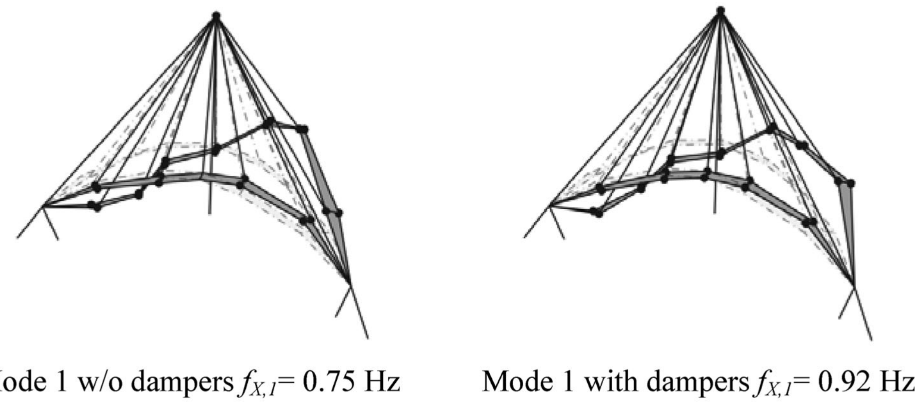

Fig. 14. Deformed shapes of the first six identified modes in the cases without and with dampers.

Table 5
Frequencies and damping ratios (%) of cable stays

Cable	*L(m)*	*Frequency (Hz)*					*ξ [%]*
(a) Case w/o antivandalism sleeves and rubber pad							
NE8	80.00	0.84	1.52	2.30	3.05	3.81	0.46
NE7	73.73	1.06	2.08	3.11	4.16	5.19	0.59
NE5	55.70	1.66	3.30	4.95	6.61	8.28	0.30
(b) Case with antivandalism sleeves and rubber pad							
NE8	80.00	0.86	1.56	2.30	3.02	3.78	0.87
NE7	73.73	1.13	2.21	3.31	4.41	5.52	0.96
NE5	55.70	1.72	3.45	5.15	6.89	8.59	0.25

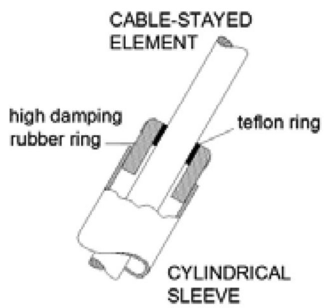

Fig. 15. Antivandalism cylindrical sleeve endowed with high damping rubber and Teflon rings.

To optimize the dynamic performance of the deck cable-stay system, the relevant interaction was investigated. In fact, possible motion coupling mechanisms could occur (Liu et al, 2013). In this respect, specific dynamic tests were addressed to identify the modal characteristics of the longest cable stays NE5, NE7, and NE8. Table 5 summarizes the results of the dynamic identification for the case without and with antivandalism sleeves that are depicted in Figure 15.

Lower frequencies of the longest cables were found to be close to the global eigenmodes of the bridge, indicating linear one-to-one internal resonances. See, for instance, the first frequencies of cables NE8 and NE7 and the first two footbridge frequencies in Table 4. To break this undesired dynamic coupling, both damping rubber and Teflon rings were installed in cylindrical antivandalism sleeves on the longest cables as depicted in Figure 15.

Both the two damping rubber half rings at the end of the sleeve and the two Teflon half rings in contact with cable introduced damping, limited stiffness, and induced small impacts in bending. Each impact can redistribute the kinetic energy of the cable between different vibration modes. When a resonance builds up, the proposed device triggers other vibration modes, and thus it modifies the frequency content of the cable response with a reduction of cable displacement amplitude (Tirelli, 2010).

4 ACCURATE FE MODEL UPDATING BASED ON EXPERIMENTAL DATA

Due to intrinsic and model uncertainties and changes during construction, differences between numerical frequencies $f_{N,i}$, and experimental frequencies $f_{X,i}$ were expected. Hence, percentage errors between experimental modal analysis (EMA) and finite-element numerical analysis (FEA) can be observed in Table 6. Thus and in agreement with step 4 of Figure 1, a FE Model Updating (MU) was performed with initial model refinement followed by a MU procedure (Brownjohn et al., 2001) described below. Note that at this stage, the MU was applied to a FE footbridge model without dampers, which were simulated later.

Table 6
Comparison between experimental ($f_{X,i}$) and numerical ($f_{N,i}$) frequencies for the footbridge w/o dampers

Mode	f_X *(Hz)*	f_N *(Hz)*	*Error (%)*
1	0.748	0.681	−8.8
2	1.065	1.003	−5.8
3	1.126	1.087	−3.5
4	1.243	1.144	−8.0
5	1.394	1.369	−1.8
6	1.510	1.518	+0.5
7	1.716	1.546	−9.9
8	1.791	1.666	−7.0
9	2.306	1.702	−26.2
10	2.364	1.984	−16.1

Table 7
Comparison between experimental ($f_{X,i}$) and numerical ($f_{N,i}$) frequencies after model refinement

Mode	f_X *(Hz)*	f_N *(Hz)*	*Error (%)*
1X – 1N	0.748	0.697	−6.8
2X – 2N	1.065	1.000	−6.1
3X – 3N	1.126	1.059	−5.9
4X – 4N	1.243	1.132	−8.9
5X – 5N	1.394	1.378	−1.1
6X – 6N	1.510	1.529	+1.3
7X – 8N	1.716	1.692	−1.4
8X – 10N	1.791	2.079	+16.1
9X – 9N	2.306	1.955	−15.2
10X – 12N	2.364	2.337	−1.1

4.1 Macro updating of the FE model

Due to some changes at the construction phase, the final structure diverged significantly from its initial design; hence, the initial FE model was modified to represent actual geometric and structural forms with as much detail as possible. The major changes were (1) the use of light-weight concrete in the cycle-track deck; (2) the adoption of five different thicknesses of concrete in the foot-track deck; (3) the addition of short and long steel diagonal members in both decks. Moreover, the modified FE model considered some issues that were left out in the initial model. In greater detail, consideration was given to the contribution of the two concrete blocks at the ends, the presence of steel sheeting beneath each concrete slab, the section variation of the tubular mast along its length owing to infill concrete, the mass of metal plates at the joints between deck segments, and a refinement of the FE model at the two end supports. To perform the model tuning and avoid diverging processes, we selected reasonable initial values of parameters. Nevertheless, as shown in Table 7, the $f_{X,i}$ values entailed by the modified FE model did not agree perfectly with the experimental results. Moreover, modal inversions occurred and MAC estimates reached an average value of 65%. Thus, it was decided to apply an optimization-based MU procedure defined in step 6 of Figure 1.

4.2 Accurate FE model tuning

The FE-based MU procedure employed relied on the inverse eigensensitivity method suggested by Friswell and Mottershead (1995). This is an indirect iterative method operating in the modal domain that, based on the difference between each component, compares numerical and experimental eigenproperties. Then, it seeks to minimize this difference by adjusting unknown parameters relevant to some significant structural properties of the FE model.

The matching procedure between numerical and experimental data was based on a least square minimization problem of a real-valued scalar objective function $F(\mathbf{p})$, which is a nonlinear function of parameter vector $\mathbf{p}$. Therefore, given the difference vector $\boldsymbol{\Delta}(\mathbf{p})$, a local minimizer $\mathbf{p}^*$ was sought for $F(\mathbf{p})$, that reads

$$F(\mathbf{p}) = \frac{1}{2} \boldsymbol{\Delta}(\mathbf{p})^T \cdot \boldsymbol{\Delta}(\mathbf{p}) \tag{5}$$

In greater detail, $\boldsymbol{\Delta}(\mathbf{p})$ defined the difference between the experimental frequencies and their corresponding numerical values (Zhou et al., 2013). Jaishi and Ren (2005) observed that eigenvalue residual in Equation (5) are enough for the optimal tuning of modal parameters. Moreover, Friswell and Mottershead (1995) highlighted that the MAC index adopted to compare shape data is not very effective when modes are close in frequency, like the case to hand. Conversely, mode-shape-based comparison becomes crucial for damage detection (Ching et al., 2006). To achieve a minimum of $F(\mathbf{p})$ in Equation (5), Powell's DL method with a trust region radius $\delta = 2$ was applied. It is a trust region method, based on combination of the classical Gauss–Newton method and the steepest descent method (Madsen et al., 2004). The objective function is approximated within a trust region of magnitude depending on the solution at the previous step. This MU procedure was successful in other realistic applications; see, for instance, Savadkoohi et al. (2011). However, to speed up the updating of the bridge to hand, we implemented the MU procedure by means of the ANSYS-APDL language script (ANSYS, 2007).

At the first stage of MU, we selected the main structural parameters that could influence the dynamic response of the footbridge. The parameters selected were the concrete elastic modulus E_{c1}; the lightweight concrete elastic modulus E_{c2}; the structural steel modulus E_s; the steel modulus of stay cables diameter 44 mm $E_{s\_stay\_44}$; the steel modulus of 60 mm cables $E_{s\_stay\_60}$; and the steel modulus of 75 mm cables $E_{s\_stay\_75}$. Moreover, we included both the concrete density ρ_1 and the lightweight concrete density ρ_2, subject to significant variation. The support bearing stiffness k was also considered and it was the only boundary condition updated. In addition, each actual deck section had variable concrete thickness due to steel sheeting. Therefore, as each deck was modeled by means of shell elements, to modify their inertial properties, the coefficients C_{pB}, C_{pC}, C_{pD}, C_{pE}, C_{pF}, and C_c were defined. Step 6 of Figure 1 was preceded by the sensitivity analysis of step 5 (Brownjohn and Xia, 2000); thus and to discard nonsensitive parameters, 15 modes and 15 parameters were considered. The resulting 15 by 15 sensitivity matrix **S** was defined as follows

$$S_{ij} \approx \frac{\Delta_i\left(p_j + \Delta p_j\right) - \Delta_i\left(p_j\right)}{\Delta p_j} \tag{6}$$

where $\Delta_i(p_j + \Delta p_j)$ represents the residual on the ith eigenvalue owing to a variation Δp_j on the jth parameter. One can note from Equation (6), that each S_{ij} term of **S** was estimated by means of finite differences. Just the following most sensitive nine parameters, i.e.,

$$E_{c1},\ E_{c2},\ E_s,\ E_{s\_stay\_44},\ \rho_1,\ \rho_2,\ C_{pB},\ C_{pD},\ C_c$$

were kept for the MU. The resulting sensitivity matrix was then evaluated at each step of the iterative optimization process, to calculate the descent direction of the trust region method.

To guarantee physically meaningful estimations of such parameters, variation limits were imposed with respect to their initial values. In agreement with previous works (Brownjohn and Xia, 2000), a maximum variation of ±15% was allowed for concrete elastic moduli E_{c1} and E_{c2}, while a ±5% was assumed for steel elastic moduli E_s and $E_{s\_stay\_44}$. A variation range of ±30% was set for concrete densities ρ_1 and ρ_2. With reference to geometric correction coefficients C_{pB}, C_{pD}, and C_c, a ±15% variation range was set according to Zivanovic et al. (2007). These variation limits represented an adequate trade-off between engineering sense and robustness of the optimization process. The accurate MU process led to the estimations reported in Table 8.

In principle, an average increase of stiffness quantities together with a decrease of density characteristics led to a positive shift of eigenvalues. Table 9 summarizes MU results.

Table 8
Changes in selected parameters

Par.	*Initial value*	*Final value*	*p (%)*
E_{c1}	35,000 MPa	38,350 MPa	+957
E_{c2}	16,000 MPa	13,600 MPa	−1500
E_s	210,000 MPa	220,500 MPa	+500
$E_{s\_stay\_44}$	165,000 MPa	156,750 MPa	−500
ρ_1	1,500 kg/m^3	1,140 kg/m^3	−2387
ρ_2	2,500 kg/m^3	1,750 kg/m^3	−3000
C_c	25.40	27.91	+990
C_{pB}	5.06	5.27	+413
C_{pD}	1.15	1.15	−043

Table 9
Comparison between experimental ($f_{X,i}$) and updated ($f_{N,i}$) frequencies after the MU

Mode	f_X *(Hz)*	f_N *(Hz)*	*Error (%)*
1X – 1N	0.748	0.738	−1.28
2X – 2N	1.065	1.048	−1.67
3X – 3N	1.126	1.099	−2.33
4X – 4N	1.243	1.179	−5.12
5X – 5N	1.394	1.437	+3.10
6X – 6N	1.510	1.608	+6.51
7X – 8N	1.716	1.761	+2.58
10X – 12N	2.364	2.435	+2.98
11X – 13N	2.512	2.502	−0.38

Table 10
MAC matrix between experimental and numerical mode shapes after the FE MU

	1X	*2X*	*3X*	*4X*	*5X*	*6X*	*7X*	*10X*	*11X*
1N	**0.99**	0.33	0.01	0.01	0.08	0.14	0.05	0.02	0.05
2N	0.00	**0.42**	0.01	0.11	0.07	0.00	0.07	0.07	0.07
3N	0.16	0.30	**0.77**	0.00	0.04	0.03	0.00	0.11	0.00
4N	0.08	0.00	0.04	**0.95**	0.12	0.11	0.27	0.02	0.00
5N	0.08	0.04	0.06	0.17	**0.38**	0.11	0.01	0.03	0.06
6N	0.08	0.07	0.00	0.02	0.00	**0.88**	0.15	0.00	0.01
8N	0.01	0.01	0.01	0.23	0.09	0.00	**0.73**	0.04	0.01
12N	0.08	0.11	0.10	0.01	0.02	0.10	0.00	**0.60**	0.27
13N	0.07	0.03	0.01	0.00	0.04	0.00	0.00	0.10	**0.49**

Note: MAC scores of corresponding mode pairs are highlighted in bold.

One can observe that the percentage error on predicted frequencies was further reduced with respect to the degree of matching obtained after the preliminary refinement summarized in Table 7. Moreover, the values of the MAC matrix reported in Table 10 corroborate the eigenmode assignment.

In greater detail and with reference to the first eigenmode, an almost perfect matching in terms of both frequency and mode shape can be appreciated.

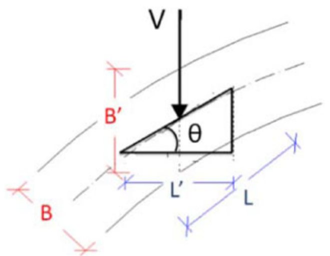

Fig. 16. Characteristic parameters of the bridge section and definition of yaw angle θ.

5 ENHANCED FE MODEL FOR WIND SIMULATIONS

To obtain a realistic FE model of the footbridge also capable of reproducing aerodynamic phenomena, it was necessary to carry out step 7 and step 8 depicted in Figure 1. The following subsections present in-depth relevant analyses.

5.1 Characterization and modeling of aerodynamic properties

It is widely agreed that long-span and/or slender bridges are very prone to aerodynamic phenomena, i.e., self-induced motion with increasing amplitude, caused by relatively low wind speeds (Simiu and Scanlan, 1996); these phenomena may induce aeroelastic instability like flutter, galloping, etc. In view of both a stability analysis and wind simulations, we define the static lift $L_s(t)$, the drag $D_s(t)$, and the moment $M_s(t)$ as

$$\begin{aligned} L_s(t) &= \frac{1}{2}\rho V^2 BLC_L(\alpha) \\ D_s(t) &= \frac{1}{2}\rho V^2 BLC_D(\alpha) \\ M_s(t) &= \frac{1}{2}\rho V^2 BLC_M(\alpha) \end{aligned} \tag{7}$$

where V defines the mean wind speed, B and L the section chord and the influence length, respectively shown in Figure 16, ρ the wind density. $C_D(\alpha)$, $C_L(\alpha)$, $C_M(\alpha)$ represent the stationary aerodynamic coefficients, β_1 the angle due to the footbridge geometry, β_2 the wind attack angle, and α the effective angle of attack as depicted in Figure 17.

In addition, the self-excited aerodynamic forces $L_{se}(t)$, $D_{se}(t)$ and $M_{se}(t)$ can be expressed as

$$\begin{aligned} L_{se}(t) = \frac{1}{2}\rho V^2 BL \Bigg(& -h_1^* \frac{i\omega z}{V} - h_2^* \frac{i\omega B\alpha}{V} + h_3^*\alpha \\ & + h_4^* \frac{\pi}{2V^{*2}}\frac{z}{B} - h_5^* \frac{i\omega y}{V} + h_6^* \frac{\pi}{2V^{*2}}\frac{y}{B} \Bigg) \end{aligned}$$

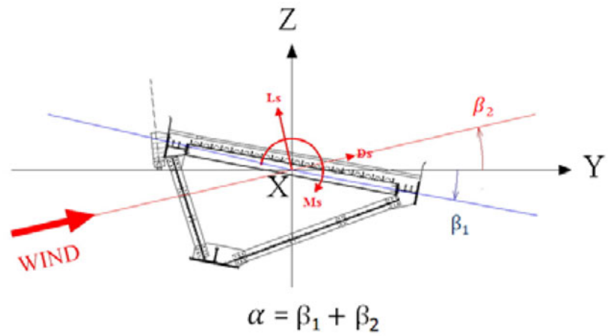

Fig. 17. Two-DoFs system and relevant angles. Static forces and moment $L_s(t)$, $D_s(t)$, and $M_s(t)$.

$$\begin{aligned} D_{se}(t) = \frac{1}{2}\rho V^2 BL \Bigg(& -p_1^* \frac{i\omega z}{V} - p_2^* \frac{i\omega B\alpha}{V} + p_3^*\alpha \\ & + p_4^* \frac{\pi}{2V^{*2}}\frac{z}{B} - p_5^* \frac{i\omega y}{V} + p_6^* \frac{\pi}{2V^{*2}}\frac{y}{B} \Bigg) \\ M_{se}(t) = \frac{1}{2}\rho V^2 B^2 L \Bigg(& -a_1^* \frac{i\omega z}{V} - a_2^* \frac{i\omega B\alpha}{V} + a_3^*\alpha \\ & + a_4^* \frac{\pi}{2V^{*2}}\frac{z}{B} - a_5^* \frac{i\omega y}{V} + a_6^* \frac{\pi}{2V^{*2}}\frac{y}{B} \Bigg) \end{aligned} \tag{8}$$

where ϖ defines the harmonic motion frequency and V^* $= V/\varpi B$ the reduced velocity. The dual kinematic quantities are as follows: y, horizontal and normal to the axis deck; z, vertical; α, torsional; h_1^*, h_2^*, h_3^*, h_4^*, h_5^*, h_6^*, p_1^*, p_2^*, p_3^*, p_4^*, p_5^*, p_6^*, a_1^*, a_2^*, a_3^*, a_4^*, a_5^*, a_6^*, etc. are flutter derivatives for lift, drag, and moment, respectively, in agreement with Zasso (1996). The relationships between Zasso (1996), and Simiu and Scanlan (1996) conventions read

$$\begin{aligned} -h_1^* &= \frac{H_1^*}{V^*}; -h_2^* = \frac{H_2^*}{V^*}; h_3^* = \frac{H_3^*}{V^{*2}}; \\ h_4^*\frac{\pi}{2V^{*2}} &= \frac{H_4^*}{V^{*2}}; -h_5^* = \frac{H_5^*}{V^*}; h_6^*\frac{\pi}{2V^{*2}} = \frac{H_6^*}{V^{*2}}; \\ -p_1^* &= \frac{P_1^*}{V^*}; -p_2^* = \frac{P_2^*}{V^*}; p_3^* = \frac{P_3^*}{V^{*2}}; \\ p_4^*\frac{\pi}{2V^{*2}} &= \frac{P_4^*}{V^{*2}}; -p_5^* = \frac{P_5^*}{V^*}; p_6^*\frac{\pi}{2V^{*2}} = \frac{P_6^*}{V^{*2}}; \\ -a_1^* &= \frac{A_1^*}{V^*}; -a_2^* = \frac{A_2^*}{V^*}; a_3^* = \frac{A_3^*}{V^{*2}}; \\ a_4^*\frac{\pi}{2V^{*2}} &= \frac{A_4^*}{V^{*2}}; -a_5^* = \frac{A_5^*}{V^*}; a_6^*\frac{\pi}{2V^{*2}} = \frac{A_6^*}{V^{*2}}; \end{aligned} \tag{9}$$

Due to the presence of hulls around the foot-track-decks, see Figure 18 referring to scale models, and the existing uncertainty in the definition of terms in both Equations (7) and (8), wind-tunnel tests were performed (Zasso et al., 2009), in agreement with step 7 of Figure 1. Thus both stationary aerodynamic

Fig. 18. Foot- and cycle-track decks located in a wind tunnel.

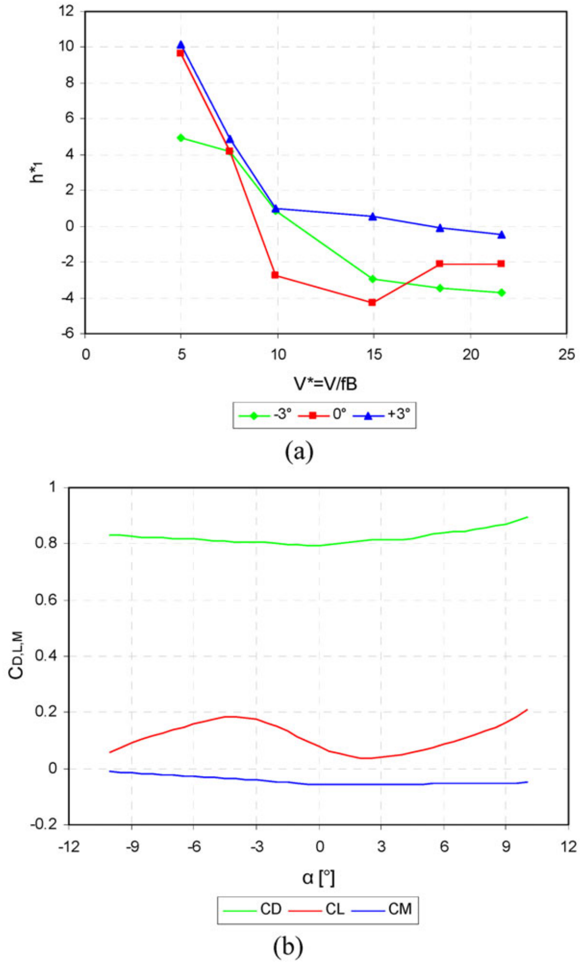

Fig. 19. Aerodynamic characteristics of the foot-track deck: (a) h_1^* flutter derivative values for different wind attack angles as a function of the reduced wind velocity V^*; (b) stationary aerodynamic coefficients C_D, C_L, and C_M vs. α.

coefficients—$C_D(\alpha)$, $C_L(\alpha)$, $C_M(\alpha)$—and flutter derivatives—a_i^*, h_i^* and p_i^*, $i = 1, \ldots, 6$—could be determined to fully characterize the aerodynamic properties of track sections, as a function of α. To this end, 1:5 scaled models of the two decks were tested in a wind tunnel as illustrated in Figure 18.

To investigate the aerodynamic behavior of the decks we measured the flutter derivatives over a wide range of reduced velocities. In this respect and as an example, Figure 19a shows the flutter derivatives h_1^* as a function of V^* for different mean angles of attack relevant to the footbridge deck with wind from the sea. The reader can see negative values of h_1^* for realistic average attack angles. This trend was expected since, as shown in Figure 19b, the aerodynamic lift coefficient $C_L(\alpha)$ exhibited a negative slope near the origin. This inevitably entails a galloping phenomenon associated with energy absorption owing to self-excited oscillation. To implement the self-excited aerodynamic forces defined in Equation (8), we used the generic *Matrix27* FE element available in the ANSYS software (ANSYS, 2007). As a result, 60 *Matrix27* elements, 30 per deck, were associated with stiffness matrices and another 60 elements with damping matrices defined in Equation (8).

For instance for the force $L_{se}(t)$, stiffness terms contained h_3^*, h_4^*, and h_6^* flutter derivatives while damping terms held h_1^*, h_2^*, and h_5^* derivatives. To estimate the critical wind speed, a stability analysis was conducted. Thus, both static and aeroelastic forces defined in Equations (8) and (9), respectively, were applied. Initially, the worst case was considered, and therefore, aeroelastic forces were applied orthogonally to the deck axes, i.e., with a yaw angle $\theta = 0$ in Figure 16. Nonetheless, both the structure spatiality and the variability of the wind attack angle α were taken into account by means of the 3D FE model. In fact, both the stationary aerodynamic coefficients and the flutter derivatives were set on the basis of the local value of α that depended on the decks' deformed shape under dead loads. The wind design velocity was set equal to 40.4 m/s for the case of wind from the sea. Structural damping was assumed to be equal to $\xi_{\text{struc}} = 0.5\%$. As a result of the stability analysis, the total damping $\xi_{\text{tot}} = \xi_{\text{struc}} + \xi_{\text{aero}}$ became negative for the first mode shape at a wind speed of about 24 m/s, as illustrated in Figure 20. This trend confirmed the galloping instability of the foot-track deck, found during wind-tunnel tests.

Thus, further analyses, with dampers, entailed damping values well above 2% for each mode, within the design wind velocity of 40.4 m/s. Finally, the FE model of the damped footbridge predicted acceleration values within the Eurocode guidelines (EN 1990, 2002) for pedestrian comfort, i.e., 0.7 m/s^2 for vertical

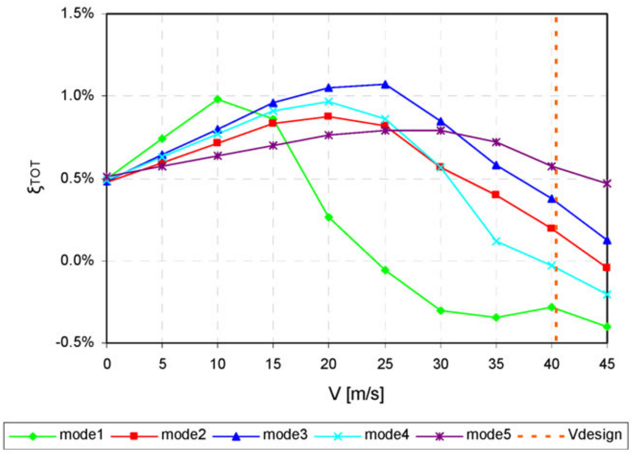

Fig. 20. Total damping ξ_{tot} as a function of the wind velocity for the footbridge without dampers.

acceleration and 0.1 m/s^2 for lateral acceleration, avoiding lock-in effects.

5.2 Stochastic modeling of the turbulent component of wind loading

The numerical simulation of the footbridge required wind time histories necessarily including turbulent conditions. In fact, the two decks are both subject to two simultaneous wind components: the static and the turbulent wind component. In particular, the turbulent or buffeting load component was applied by Lift, Drag, and Moment forces:

$$
\begin{aligned}
L_b(t) &= \frac{1}{2}\rho V(z)^2 B \left\{2C_L(\alpha)\frac{v'(t)}{V(z)} + \left[C'_{L|\alpha}(\alpha) - C_D(\alpha)\right]\frac{w'(t)}{V(z)}\right\} \\
D_b(t) &= \frac{1}{2}\rho V(z)^2 B \left\{2C_D(\alpha)\frac{v'(t)}{V(z)} + \left[C'_{D|\alpha}(\alpha) - C_L(\alpha)\right]\frac{w'(t)}{V(z)}\right\} \\
M_b(t) &= \frac{1}{2}\rho V(z)^2 B^2 \left\{2C_M(\alpha)\frac{v'(t)}{V(z)} + C'_{M|\alpha}(\alpha)\frac{w'(t)}{V(z)}\right\}
\end{aligned}
\tag{10}
$$

where ρ is the air density; u', v', and w' define the stationary stochastic components with zero mean of the turbulence; $C_L(\alpha)$, $C_D(\alpha)$, $C(\alpha)$ are the static coefficients; $C_{L|\alpha}{}'(\alpha)$, $C_{D|\alpha}{}'(\alpha)$, $C_{M|\alpha}{}'(\alpha)$ are the buffeting coefficients; and $V(z)$ is the mean velocity in the mainstream direction defined by the Y axis in Figure 17. In the turbulent boundary layer, the mean wind velocity is assumed to be constant and has a logarithmic profile defined as

$$V(z) = v^* \frac{1}{k} ln \frac{z}{z_0} \tag{11}$$

where $v^* = \sqrt{\tau_0/\rho} = 1.76$ m/s defines the friction velocity, τ_0 is the shear stress at the ground surface and ρ is the air density assumed 1.25 kg/m^3; k is Von Karman's constant equal to 0.4; z is the height above ground and z_0 is the roughness length depending on terrain type (Simiu and Scanlan, 1996; Dyrbye and Hansen, 1997).

If we assume the Cartesian reference system X, Y, Z, with X along the deck axis, Y orthogonal to the X axis, and Z in the vertical direction as depicted in Figure 17, the 3D wind velocity components associated to a point in space read

$$
\begin{aligned}
u(t) &= u'(x, y, z, t) \\
v(t) &= V(z) + v'(x, y, z, t) \\
w(t) &= w'(x, y, z, t)
\end{aligned}
\tag{12}
$$

The correlation among u', v', and w' is assumed to be weak and in practice can be omitted (Simiu and Scanlan, 1996); thus, three 1D multivariate stochastic uncorrelated processes can be assumed point-wise and a multivariate wind field has to be generated. In this respect Deodatis (1996) proposed a simulation algorithm capable of generating stationary, multivariate stochastic processes according to a defined cross-spectral density matrix linked to a specific climatic zone (CNR-DT 207/2008, 2008; EN 1191-1-4 2005). According to Deodatis' notation, a 1D multivariate Gaussian process with zero mean can be characterized by the following cross-spectral density function:

$$S^0(\omega) = \begin{bmatrix} S^0_{11}(\omega) & \cdots & S^0_{1n}(\omega) \\ \vdots & \ddots & \vdots \\ S^0_{n1}(\omega) & \cdots & S^0_{nn}(\omega) \end{bmatrix} \tag{13}$$

where n is the number of simulation points; $S^0_{jj}(\omega) = S_j(\omega)$, $j = 1, \ldots, n$ is the power spectral density function of the signal $f_j(t)$ to be generated although $S^0_{jk}(\omega) = \sqrt{S_j(\omega)S_k(\omega)}\gamma_{jk}(\omega), j, k = 1, \ldots, n$ is the cross power spectral density function with $\gamma_{jk}(\omega)$ coherence function between $f_j(t)$ and $f_k(t)$. $\mathbf{S}^0(\omega)$ can be decomposed into the product of two triangular matrices with Cholesky decomposition:

$$\mathbf{S}^0(\omega) = \mathbf{H}(\omega)\mathbf{H}^{T*}(\omega) \tag{14}$$

where $\mathbf{H}(\omega)$ is a lower triangular matrix and T^*. defines its complex conjugate transposed matrix. As the number N of frequency intervals is such that $N \to \infty$, the

Table 11
Numerical simulations analyzed for static and dynamic wind loads

NS and description		Static component of the wind load	Dynamic component of the wind load
A	**Orthogonal wind**	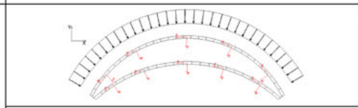	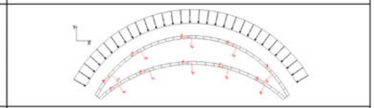
		$C_D(\alpha,0),\ C_L(\alpha,0),\ C_M(\alpha,0)$ B, L	$H_i^* = H_i^*(\alpha,0,K),\ A_i^* = A_i^*(\alpha,0,K)$ B, L
C	**Cosine rule and skew wind theory**	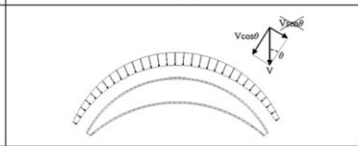	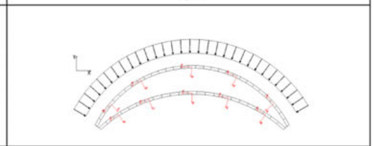
		$C_D(\alpha,\theta)=C_D(\alpha,0)\cos^2\theta$ $C_L(\alpha,\theta)=C_L(\alpha,0)\cos^2\theta$ $C_M(\alpha,\theta)=C_M(\alpha,0)\cos^2\theta$ B, L	$H_i^* = H_i^*(\alpha,0,K_\perp),\ A_i^* = A_i^*(\alpha,0,K_\perp)$ $V_\perp = U\cos\theta,\ V_{red,\perp} = \frac{U\cos\theta}{fB},\ K_\perp = \frac{2\pi}{V_{red\perp}}$
D		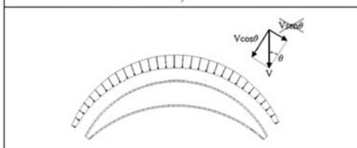	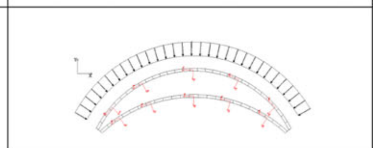
		$C_D(\alpha,\theta)=C_D(\alpha,0)\cos^2\theta$ $C_L(\alpha,\theta)=C_L(\alpha,0)\cos^2\theta$ $C_M(\alpha,\theta)=C_M(\alpha,0)\cos^2\theta$ B, L	$H'^*_i = H_i^*(\alpha,0,K')/\cos^2\theta$ $A'^*_i = A_i^*(\alpha,0,K')/\cos^2\theta$ $V_{red}' = \frac{V}{fB'} = \frac{V\cos\theta}{fB},\ K' = \frac{2\pi}{V_{red}'}$
G	**Wind Y**	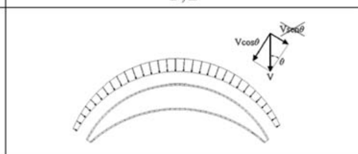	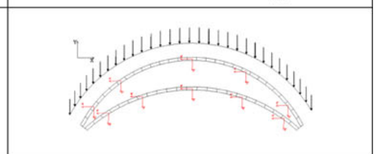
		$C_D(\alpha,\theta)=C_D(\alpha,0)\cos^2\theta$ $C_L(\alpha,\theta)=C_L(\alpha,0)\cos^2\theta$ $C_M(\alpha,\theta)=C_M(\alpha,0)\cos^2\theta$ B, L	$H'^*_i = H_i^*(\alpha,0,K')/\cos^2\theta$ $A'^*_i = A_i^*(\alpha,0,K')/\cos^2\theta$ $V_{red}' = \frac{V}{fB'} = \frac{V\cos\theta}{fB},\ K' = \frac{2\pi}{V_{red}'}$ *Matrix27* elements along Y direction
H		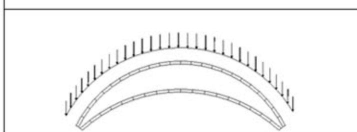	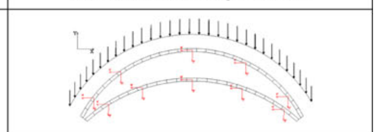
		$C_D(\alpha,0),\ C_L(\alpha,0),\ C_M(\alpha,0)$ B', L'	$H'^*_i = H_i^*(\alpha,0,K')$ $A'^*_i = A_i^*(\alpha,0,K')$ $V_{red}' = \frac{V}{fB'} = \frac{V\cos\theta}{fB},\ K' = \frac{2\pi}{V_{red}'}$ *Matrix27* elements along Y direction
I		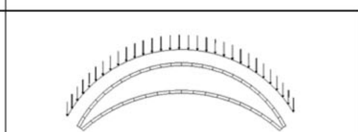	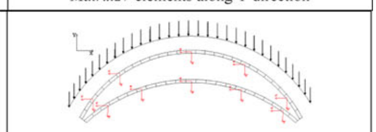
		$C_D(\alpha,0),\ C_L(\alpha,0),\ C_M(\alpha,0)$ B', L'	$H'^*_i = H_i^*(\alpha,0,K')/\cos^2\theta$ $A'^*_i = A_i^*(\alpha,0,K')/\cos^2\theta$ $V_{red}' = \frac{V}{fB'} = \frac{V\cos\theta}{fB},\ K' = \frac{2\pi}{V_{red}'}$ *Matrix27* elements along Y direction

simulated stochastic process is asymptotically Gaussian owing to the central limit theorem, so samples of the simulated stochastic process can be expressed as

$$f_j(t) = 2\sqrt{\Delta\omega} \sum_{m=1}^{j} \sum_{l=1}^{N} \left| H_{jm}(\omega_{ml}) \right| \cdot \cos\left(\omega_{ml} t - \theta_{jm}(\omega_{ml}) + \varphi_{ml}\right), \; j = 1, 2, \ldots, n. \tag{15}$$

The Von Karman cross-spectral density function was adopted both for the horizontal and the vertical component of turbulence, for a return period $T_R = 500$ years (Dyrbye and Hansen, 1997). As a result, we considered

$$\frac{f S_v(z, f)}{\sigma_v^2(z)} = \frac{4 n_L}{\left(1 + 70.8 n_L^2\right)^{5/6}}, \; n_L = \frac{f L_v}{V(z)} \tag{16}$$

where f is the frequency in Hz; $\sigma_v^2(z)$ is the variance of the turbulence component; n_L is the nondimensional frequency; L_v is the height-dependent length scale of turbulence. In particular, σ and L were taken from National Standards (CNR-DT 207/2008). The coherence function in nondimensional form used in Equation (17) was taken from Dyrbye and Hansen (1997):

$$\gamma(\Delta y, f) = \exp\left(-C \frac{\Delta y f}{V}\right) \tag{17}$$

where C is a coefficient defined in CNR-DT 207/2008 (2008).

6 FE MODEL UPDATING ACCORDING TO THE SKEWED WIND THEORY AND VALIDATION

Preliminary simulation based on the updated FE model developed in Section 4.2 assigned both aerodynamic and flutter coefficients orthogonal to footbridge decks. Nonetheless, in reality the wind is not always a normal wind, and therefore, other assumptions were considered to carry out step 8 of Figure 1. In greater detail, we analyzed the cosine rule (Tanaka and Davenport, 1982), the skew wind theory (Simiu and Scanlan, 1996), and their combinations. With regard to Equations (7), (8), and (9) of Section 5.1, coefficients for both the static and the self-excited aerodynamic component of drag, lift, and moment forces were considered as shown in Table 11. All analyses were performed on the enhanced FE updated model defined in Section 4.2; moreover, the analyses considered the worst wind condition from the sea. Wind loads were applied at specific points called aerodynamic nodes; there were 30 nodes per deck subject to three wind components each. In greater detail, the three numerical simulations (NSs) analyzed for the static components of Equation (7) are listed herein, and refer to parameters shown in Table 11. (A) Wind orthogonal to the X axis of each deck: in this NS the wind acted along the orthogonal direction, i.e., with a yaw angle $\theta = 0°$, see Figures 16 and 17, and steady-state aerodynamic coefficients were the ones obtained during wind-tunnel tests (Zasso et al., 2009). (C) and (D) NSs based on the Cosine rule application: only the velocity component normal to each deck X axis was taken into account, whatever the direction of the wind. This rule entailed that given a particular wind distribution, only the component $V\cos(\theta)$ was considered effective; see in this respect Figure 16 to understand convention for angle θ. (G), (H), and (I) NSs based on wind in the Y direction: steady-state aerodynamic coefficients were considered for $\theta = 0°$, but they were referred to an elongated section of width B', depicted in Figure 16. Besides, the influence area for each concentrated load varied as a function of θ. So we considered the segment of influence to be orthogonal to the line of flow, i.e., $L' = L\cos\theta$. In a first step, only the static component of the wind was applied and with reference to the three NSs listed above, we can draw the following conclusions: (1) NS #1 and NS #2 showed some difference with regard to displacement/rotation as a function of the yaw angle θ. Maximum deviation was at the deck center with 1.71 mm for displacement and 0.00458° for rotation; (2) the footbridge response did not exhibit high sensitivity to the static wind component. Along the same line, a few NSs referring to wind components, linked to aerodynamic action, were considered and are listed here:

Table 12
Critical velocity and frequency for different numerical simulations

	Description of NSs		V_{cr} *(m/s)*	f_{cr} *(Hz)*
A	Orthogonal wind	-	24.41	0.7244
C	Cosine rule and skew wind theory	Static and dynamic application of the cosine rule	28.33	0.7244
D		Static application of the cosine rule and dynamic application of the skew wind theory	26.84	0.7215
G	Wind Y	NS #1	26.50	0.7220
H		NS #2	27.40	0.7230
I		NS #3	26.50	0.7219

Note: Labels in column one refer to entries of Table 11.

Table 13
Percentage errors between experimental and numerical root mean square of acceleration signals

	NS #1 Normal wind		*NS #2 Cosine rule and skew wind*		*NS #3 Wind Y NS #2*	
	August	*April*	*August*	*April*	*August*	*April*
Accelerometer	*Err (%)*		*Err (%)*		*Err (%)*	
M1	121.60	136.64	71.94	115.13	119.31	174.05
M2	−4.80	−2.015	−20.49	−4.00	−7.58	11.40
M3	−3.66	9.74	−20.78	5.59	−5.26	26.17
M4	−6.58	10.26	−25.37	3.14	−8.80	25.81
M5	−0.45	41.05	−16.07	39.50	−1.81	63.27
M6	0.53	17.78	−16.70	14.41	−3.49	32.54
M7	−24.73	2.072	−34.90	3.70	−25.70	18.31
M8	21.256	48.30	−1.47	41.53	16.12	66.72

Note: Err refers to Equation (18).

A—Normal wind: wind acted with a yaw angle $\theta = 0^\circ$ and aerodynamic coefficients determined during wind-tunnel tests; the section width and the influence length considered were B and L, respectively.

C—Application of the cosine rule to both components of Figure 16, where we considered effective for both static and dynamic response only the velocity component defined by $V \cos\theta$.

D—Application of the cosine rule for the static wind component and of skew wind theory for the dynamic component; the assembly of aerodynamic matrices was made in agreement with the Scanlan theory (Simiu and Scanlan, 1996). Besides, *Matrix27* elements were arranged in the direction orthogonal to the deck X axis, to take into account the self-excited wind component capable of inducing rotation along that specific direction.

G, H, I—Wind direction Y. In this situation, we considered three different NSs obtained from the combination of two static and two dynamic load types. With regard to the static part: (1) we applied the cosine rule; (2) we used static coefficients for $\theta = 0^\circ$ but employed both B' and L' dimensions. Conversely and with reference to the dynamic part: (1) we used flutter derivative coefficients according to the Scanlan theory, with *Matrix27* elements oriented along the Y direction; (2) we considered flutter derivative coefficients for $\theta = 0^\circ$ but referred to a reduced velocity V', with *Matrix27* elements oriented along direction Y defined in Figure 17. Table 12 collects critical wind speeds related to each NS considered. In detail, critical velocity V_{cr} values correspond to galloping aerodynamic instability; moreover, NS A entails the most conservative estimation of V_{cr} equal to 24.41 m/s. In the case of the Pescara footbridge the yaw angle θ approaches values of 54° close to the end. Experimental tests on the Tsing Ma Bridge (Zhu et al., 2002a, b) showed that for a low reduced velocity, approximately $V^* < 8 \div 11$, the application of the skew wind theory provided results very close to experimental values. Also the so-called “Wind Y” NSs of Table 12 provided V_{cr} values always greater than that in NS A. In particular, it is interesting to compare NSs G and I. The difference between G and I is in the assumptions related to application of the static load component of Equation (7) although the assembly of *Matrix27* is the same. Results from numerical investigation showed that $V_{cr,G} = 26.50$ m/s although V_{cr} reached its maximum value of 28.33 m/s for NS C and a minimum value of 24.41 m/s for NS A.

Therefore, we can conclude that the footbridge is sensitive to galloping phenomena, but is not very sensitive to the wind load application or to the direction in which aerodynamic stiffness and damping matrices are active; in addition, the skew wind theory seemed to provide the best results.

The third part of the simulations involved buffeting analyses with wind loads described by Equation (10). In this respect Table 13 summarizes results provided by three time history analyses from the FE model in the ANSYS software (ANSYS, 2007), together with actual records of two wind events—August and April—provided by accelerometers shown in Figure 4. In detail, we considered two wind histories: (1) a history recorded on August 29, 2010 between 00:48:31 and 00:58:47 characterized by V = 16.46 m/s; and (2) a history recorded on April 13, 2011 between 05:35:31 and 05:45:30 with V = 19.10 m/s. As a result, the interference between pedestrian and wind loading was minimized. Percentage errors between experimental and

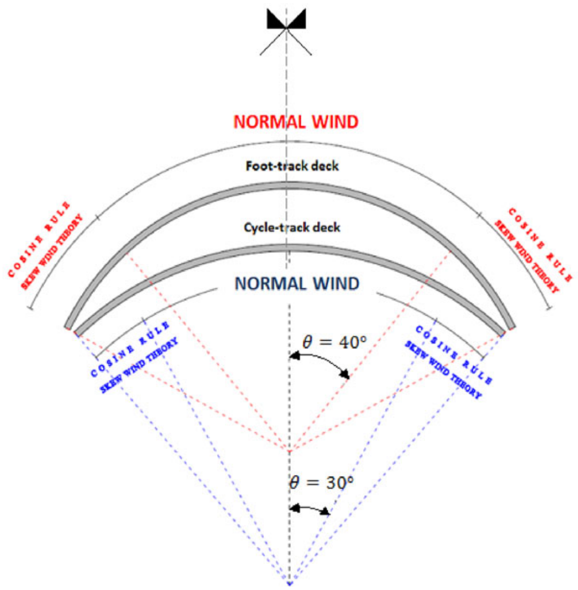

Fig. 21. Assumptions of aerodynamic behavior as a function of the yaw angle θ.

numerical root mean square (RMS) of acceleration signals were defined according to Equation (18):

$$\mathrm{Err} = \frac{\mathrm{RMS}_{\mathrm{num}} - \mathrm{RMS}_{\mathrm{exp}}}{\mathrm{RMS}_{\mathrm{exp}}} \cdot 100 \qquad (18)$$

Results show an underestimation of acceleration data from the FE model subjected to the August wind history and an overestimation when the model was subject to the April wind, with the exception of the accelerometers M1 and M8. This was mainly due to the different direction of the actual wind histories and consequently differing damper activation. In fact in terms of damping, the positive sign of errors on RMS means that the FE model is less stiff than the actual bridge. The acceleration trend, in correspondence with accelerometers located near the access ramp, differs appreciably and is overestimated. Moreover, for accelerometers M1 and M8, located in the foot- and cycle-track decks respectively, see Figure 4, NS #2 provides the smaller percentage error. In general, it can be concluded that results for the wind history of August are sufficiently favorable, as the error on RMS is always less than 26%, except for the accelerometer M7 in NS #2. NS #1 is the closest to recorded data in terms of errors on RMS. With regard to the April wind history, recorded acceleration values are overestimated, partly because the average wind speed is higher than that of the August wind. Errors on RMS referred to accelerometers M1 and M8 are high too.

The configuration that least overestimates M1 and M8 accelerometers is NS #2; the error at accelerometer M5, also located close to one end, is high. In addition, errors on RMS show that for the wind of April, NS #2 provides a better approximation of the actual wind distribution. In sum, to better agree with recorded data, we assumed a hybrid deployment of steady-state coefficients and flutter derivatives as a function of the yaw angle θ according to Figure 21 and Table 14.

This distribution will be further used for the FE model to be employed in a reliability analysis afterward. Finally, the enhanced FE model provided by step 8 of Figure 1 could also permit one to check the role of aerodynamic and aeroelastic effects not included in the present study, e.g., vortex shedding or wake effects (Cigada et al. 1997, Diana et al., 2006, Caracoglia et al., 2009).

Table 14
Expressions for steady-state coefficients and flutter derivatives used

Deck	*Angle θ*	*Static polar*	*Flutter derivatives*
Foot deck	$-54.69^\circ \le \theta < -40^\circ$ $40^\circ < \theta \le 54.69^\circ$	$C_{D,L,M} = C_{D,L,M}(\alpha,0)\cdot\cos^2\theta$	$A_i^* = A_1^*(0,\alpha,K')/\cos^2\theta$ $H_i^* = H_i^*(0,\alpha,K')/\cos^2\theta$
	$-40^\circ \le \theta \le 40^\circ$	$C_{D,L,M} = C_{D,L,M}(\alpha,0)$	$A_i^* = A_1^*(0,\alpha,K)$ $H_i^* = H_1^*(0,\alpha,K)$
Cycle deck	$-36.56^\circ \le \theta < -30^\circ$ $30^\circ < \theta \le 36.56^\circ$	$C_{D,L,M} = C_{D,L,M}(\alpha,0)\cdot\cos^2\theta$	$A_i^* = A_1^*(0,\alpha,K')/\cos^2\theta$ $H_i^* = H_i^*(0,\alpha,K')/\cos^2\theta$
	$-30^\circ \le \theta \le 30^\circ$	$C_{D,L,M} = C_{D,L,M}(\alpha,0)$	$A_i^* = A_1^*(0,\alpha,K)$ $H_i^* = H_1^*(0,\alpha,K)$

7 CONCLUSIONS

To obtain a realistic FE model of the twin deck curved cable-stayed Ponte del Mare steel footbridge, we have presented a rational process of modeling and simulation based on identification, model updating, and validation. As a result, the modal characteristics of the footbridge were properly extracted from signals produced by ambient vibration via the stochastic subspace identification algorithm; although similar quantities were identified by free-decay signals produced by impulsive excitation by means of the ERA. The subsequent modal updating was able to reproduce the response of the footbridge subjected to realistic wind loading conditions. Moreover, the FE was further updated in the time domain, by taking into account the effect of the curved deck layout both on the flutter derivatives and on the stationary aerodynamic coefficients of the deck sections. The analysis highlighted that for this Case Study, the Skew Wind theory was appropriate at the two ends of the decks, although the Normal Wind theory provided more realistic results at the central parts of the two decks.

ACKNOWLEDGMENTS

This work is supported by funds of the European Project HITUBES: "Design and Integrity Assessment of High Strength Tubular Structures for Extreme Loading Conditions," Grant N. RFSR-CT-2008-00035. Moreover, the authors are grateful to Dr. Zasso and his group for wind-tunnel tests carried out at the Politecnico di Milano.

REFERENCES

Adeli, H. & Jiang, X. (2006), Dynamic fuzzy wavelet neural network model for structural system identification, *Journal of Structural Engineering*, **132**(1), 102–11.

Allemang, R. J. (2002), The modal assurance criterion (MAC): twenty years of use and abuse, *Proceedings 20th International Modal Analysis Conference*, Los Angeles, CA, pp. 397–405.

ANSYS (2007), *Documentation for ANSYS—Release 11.0*. Copyright SAS IP, Inc., SAS Campus Drive, Cary, NC.

Brownjohn, J. M. & Xia, P. Q. (2000), Dynamic assessment of curved cable-stayed bridge by model updating, *Journal of Structural Engineering*, **126**(2), 252–60.

Brownjohn, J. M. W., Xia, P. Q., Hao, H. & Xia, Y. (2001), Civil structure condition assessment by FE model updating, *Finite Elements in Analysis and Design*, **37**(10), 761–75.

Bruno, D., Greco, F. & Lonetti, P. (2008), Dynamic impact analysis of long span cable-stayed bridges under moving loads. *Engineering Structures*, **30**(4), 1160–77.

Bursi, O. S. Kumar A. (2011), *Design and Integrity Assessment of High Strength Tubular Structures for Extreme Loading Conditions*, Final Report, HITUBES Project, Contr. No: RFSR-CT-2008-00035, Research Fund for Coal and Steel, European Commission, Brussels.

Caracoglia, L., Noè, S. & Sepe, V. (2009), Nonlinear computer model for the simulation of lock-in vibration on long-span bridges, *Computer-Aided Civil and Infrastructure Engineering*, **24**(2), 130–44.

Carden, E. P. & Brownjohn, J. M. W. (2008), Fuzzy cluster of stability diagrams for vibration-based structural health monitoring, *Computer-Aided Civil and Infrastructure Engineering*, **23**(5), 360–72.

Ceravolo, R. (2009), Time–frequency analysis, in C. Boller, F. K. Chang, and Y. Fujino (eds.), *Encyclopedia of Structural Health Monitoring,* Wiley & Sons Ltd, Chichester, United Kingdom, DOI: 10.1002/9780470061626.shm047.

Ceravolo, R. & Abbiati, G. (2009), SDIT Release 3.1 User's Manual. *Structural Identification Toolbox for Matlab*, Politecnico di Torino, Turin, Italy.

Ceravolo, R. & Abbiati, G. (2013), Time domain identification of structures: a comparative analysis of output-only methods, *Journal of Engineering Mechanics (ASCE)*, **139**(4), 537–44.

Ceravolo, R., Tondini, N., Abbiati, G. & Kumar, A. (2012), Dynamic characterization of complex bridge structures with passive control systems, *Structural Control and Health Monitoring*, **19**(4), 511–34.

Ching, J., Muto, M. & Beck, J. L. (2006), Structural model updating and health monitoring with incomplete modal data using Gibbs sampler, *Computer-Aided Civil and Infrastructure Engineering*, **21**(4), 242–57.

Cigada, A., Diana, G., Falco, M., Fossati, F. & Manenti, A. (1997), Vortex shedding and wake-induced vibrations in single and bundle cables, *Journal of Wind Engineering and Industrial Aerodynamics*, **72**, 253–63.

CNR-DT 207/2008 (2008), *Istruzioni per la valutazione delle azioni e degli effetti del vento sulle costruzioni*. Roma.

Dallard, P., Fitzpatrick, A. J., Flint, A., Le Bourva, S., Low, A., Ridsdill Smith, R. M. & Willford, M. (2001), The London Millennium footbridge, *The Structural Engineer*, **79**(2), 17–33.

Deodatis, G. (1996), Simulation of ergodic multivariate stochastic processes, *Journal of Engineering Mechanics*, **122**(8), 778–87.

Diana, G., Resta, F., Belloli, M. & Rocchi, D. (2006), On the vortex shedding forcing on suspension bridge deck, *Journal of Wind Engineering and Industrial Aerodynamics*, **94**(5), 341–63.

Dyrbye, C. & Hansen, S. O. (1997), *Wind Loads on Structures*, John Wiley & Sons, Chichester, United Kingdom.

EN 1990 (2002), *Eurocode EN1990: 2002: Basis of Structural Design—prAnnex A2.* European Committee for Standardization, Brussels, Belgium.

EN 1991-1-4 (2005), *Eurocode 1: Actions on Structures—Part 1–4: General Actions-Wind Actions*. CEN, Brussels, Belgium.

Friswell, M. I. & Mottershead, J. E. (1995), *Finite Element Model Updating in Structural Dynamics*, Kluwer Academic Publishers, Norwell, MA.

Gentile, C. & Martinez y Cabrera, F. (2004), Dynamic performance of twin curved cable-stayed bridges, *Earthquake Engineering and Structural Dynamics*, **33**(1), 15–34.

Hazra, B., Sadhu, A., Roffel, A. J. & Narasimhan, S. (2012), Hybrid time–frequency blind source separation towards ambient system identification of structures. *Computer-Aided Civil and Infrastructure Engineering*, **27**(5), 314–32.

He, X., Moaveni, B., Conte, J. P., Elgamal, A. & Masri, S. F. (2007), Modal identification study of Vincent Thomas bridge using simulated wind-induced ambient vibration data, *Computer-Aided Civil and Infrastructure Engineering*, **23**(5), 373–88.

Jaishi, B. & Ren, W. (2005). Structural finite element model updating using ambient vibration test results, *Journal of Structural Engineering*, **131**(4), 617–28.

Juang, J. N. & Pappa, R. S. (1984), An eigensystem realisation algorithm (ERA) for modal parameter identification and modal reduction, *NASA/JPL Workshop on Identification and Control of Flexible Space Structures*, **8**(5), 620–27.

Khelifa, M. R. & Guessasma, S. (2013), New computational model based on finite element method to quantify damage evolution due to external sulphate attack on self-compacting concretes, *Computer-Aided Civil and Infrastructure Engineering*, **28**(4), 260–72.

Liu, M.-Y., Zuo, D. & Jones, N. P. (2013). Analytical and numerical study of deck-stay interaction in a cable-stayed bridge in the context of field observations. *Journal of Engineering Mechanics*, **139**(11), 1636–52.

Madsen, K., Nielsen, H. B. & Tingleff, O. (2004), Methods for non-linear least square problems. Informatics and mathematical modelling. Technical University of Denmark, Lyngby, Denmark.

Magalhães, F., Cunha, A. & Caetano, E. (2008), Dynamic monitoring of a long span arch bridge, *Engineering Structures*, **30**(11), 3034–44.

MATLAB (2003), *Computer Software*, Version 6.5.1, The MathWorks Inc., Natick, Massachusetts.

Moaveni, B., Conte, J. P. & Hemez, F. M. (2009), Uncertainty and sensitivity analysis of damage identification results obtained using finite element model updating, *Computer-Aided Civil and Infrastructure Engineering*, **24**(5), 320–34.

Molinari, M., Savadkoohi, A. T., Bursi, O. S., Friswell, M. I. & Zonta, D. (2009), Damage identification of a 3D full scale steel—concrete composite structure with partial-strength joints at different pseudo-dynamic load levels, *Engineering Structural Dynamics*, **38**(1), 1219–36.

Newmark, N. M. (1959), A method of computation for structural dynamics, *Journal of the Engineering Mechanics Division, ASCE*, **85**, 67–94.

Savadkoohi, A. T., Molinari, M., Bursi, O. S. & Friswell, M. I. (2011), Finite element model updating of a semi-rigid moment resisting structure, *Structural Control Health Monitoring*, **18**(2), 149–68.

Simiu, E. & Scanlan, R. H. (1996), *Wind Effects on Structures,* 3rd edn. Wiley, New York.

Strasky, J. (2011), Stress ribbon and cable-supported pedestrian bridges. ICE Publishing, Thomas Telford, London. ISBN-10: 0727741462. Limited.

Swensson, H. (2012), *Cable-stayed Bridges*. Ernst & Sohn Gmbh and Co., Berlin, Germany.

Tanaka, H. & Davenport, A. G. (1982), Response of taut ship modules to turbulent wind, *Journal of Engineering Mechanics, ASCE*, **108**(1), 33–49.

Tirelli, D. (2010), *Vibration Mitigation of Stay Cables Using a State Switched Inducer,* Exploratory Research Projects 2010, IPSC, JRC, European Commission, Ispra, Italy.

Troyano, L. F., Armisen, J. M. & Suarez, M. A. A. (1998), The inclined towers of the Ebro and Lerez bridge. *Structural Engineering International*, **8**(4), 258–60.

Van Overschee, P. & De Moor, B. (1996), *Subspace Identification for Linear Systems: Theory—Implementation—Applications*, Kluwer Academic Press, Dordrecht, The Netherlands.

Welch, P. D. (1967), The use of Fast Fourier Transform for the estimation of Power Spectra: a method based on time averaging over short modified periodograms, *IEEE Transactions on Audio Electro-Acoustic*, **15**(2), 70–73.

Zasso, A. (1996), Flutter derivatives: advantage of a new representation convention, *Journal of Wind Engineering and Industrial Aerodynamics*, **60**, 35–47.

Zasso, A., Belloli, M. & Muggiasca, S. (2009), Wind tunnel study on the Pescara footbridge, in *FACWE 5*, Florence, Italy, July 19–23.

Zhou, L., Yan, G. & Ou, J. (2013), Response surface method based on radial basis functions for modeling large-scale structures in model updating, *Computer-Aided Civil and Infrastructure Engineering*, **28**(3), 210–26.

Zhu, L. D., Xu, Y. L. & Xiang, H. F. (2002a), Tsing Ma bridge deck under skew winds-part II: flutter derivatives, *Journal of Wind Engineering and Industrial Aerodynamics*, **90**(7), 807–37.

Zhu, L. D., Xu, Y. L., Zhang, F. & Xiang, H. F. (2002b), Tsing Ma bridge deck under skew winds. Part I: aerodynamic coefficients, *Journal of Wind Engineering and Industrial Aerodynamics*, **90**(7), 781–805.

Zivanovic, S., Pavic, A. & Reynolds, P. (2007), Finite element modelling and updating of a lively footbridge: the complete process, *Journal of Sound and Vibrations*, **301**(1), 126–45.